Additive Manufacturing 60 (2022) 103266

Contents lists available at ScienceDirect

Additive Manufacturing

journal homepage: www.elsevier.com/locate/addma

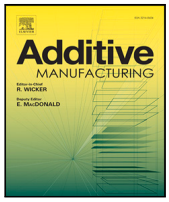

Research paper

Concurrent modeling of porosity and microstructure in multilayer three-dimensional simulations of powder-bed fusion additive manufacturing of INCONEL 718

Robert Laskowski [a,*], Rajeev Ahluwalia [a], Gary Teh Wei Hock [b], Choy Sing Ying [c], Chen-Nan Sun [c], Pei Wang [b], Dennis Tan Cheng Cheh [b], Nai Mui Ling Sharon [c], Guglielmo Vastola [a,*], Yong-Wei Zhang [a]

[a] A*STAR Institute of High Performance Computing (IHPC), 1 Fusionopolis Way, #16-16, Connexis, Singapore 138632, Singapore
[b] A*STAR Institute of Materials Research and Engineering (IMRE), 2 Fusionopolis Way, Singapore 138634, Singapore
[c] A*STAR Singapore Institute of Manufacturing Technology (SIMTech), 2 Fusionopolis Way, Singapore 138634, Singapore

ARTICLE INFO

Keywords:
Additive manufacturing
Modeling
Microstructure structure
INCONEL 718

ABSTRACT

Laser powder-bed fusion (L-PBF) additive manufacturing is a complex process whereby a laser selectively scans over layers of powder, inducing local melting and consolidation of solid metal. A key bottleneck issue which prevents L-PBF from further industrial adoption is the low repeatability of the process across different printers and powder batches. To explore and address the challenges of process repeatability, high-fidelity comprehensive physics-based modeling is desirable because it allows fast exploration of the process parameters space by simulations rather than by trial-and-error experiments. In this work, we present a complete framework which is capable of modeling defects (porosity) as well as microstructure explicitly in three dimensions and for multiple layers, effectively demonstrating explicit L-PBF of a digital cube of material at millimeter scale. The phase field method is coupled to the Lattice Boltzmann method, and the framework is used to model both the solid/liquid phase transitions as well as grain nucleation and growth. Explicit parallel scheme allows to run multiple simulations in a reasonable time and explore the role of process parameters on porosity and microstructure concurrently. After model calibration using experimentally-printed and characterized samples, the model was deployed across multiple parameter combinations. The predicted porosity and microstructure agreed well with the experiments. Our framework provides a practical demonstration of digitalization of the L-PBF process and paves the way for assessing process quality and repeatability by computer modeling and simulations.

1. Introduction

As global manufacturing adapts to decentralization, digitalization emerges as a promising route [1] to address its challenges. For the case of additive manufacturing (AM), digitalization has the potential to enable manufacturers to develop their raw materials, printing equipment, and part designs digitally rather than by experimental trial-and-error. Such paradigm shift has evident advantages in terms of quality control for decentralized supply chains because it streamlines process development and removes physical barriers.

Achieving digitalization of the laser powder-bed fusion (L-PBF) AM process is a very ambitious task. The challenge arises from the coupling between multiple physical processes playing a key role, including the absorption of laser radiation into the material, large heating and cooling rates, complex fluid dynamics in the melt pool, rapid solidification and concurrent emergence of residual stresses [2]. Modeling efforts at the scale of the powder have predominantly focused on single-track and melt pool behavior. Khairallah et al. have employed a massively parallel Lagrangian–Eulerian framework where ray-tracing is coupled to fluid dynamics and phase transitions on the fly [3]. Recently, such framework has explicitly resolved the details of keyhole porosity formation [4], paving the way for digital assessment of defect formation. Efficient graphical processing unit (GPU) implementation of such framework was demonstrated by Zakirov et al. [5], whereby fluid dynamics is solved using the Lattice Boltzmann Method (LBM). Other notable implementations include that of Yan et al., which recently showed the digitalization of powder flight due to entrapment

* Corresponding authors.
E-mail addresses: rolask@ihpc.a-star.edu.sg (R. Laskowski), vastolag@ihpc.a-star.edu.sg (G. Vastola).

https://doi.org/10.1016/j.addma.2022.103266
Received 5 May 2022; Received in revised form 3 October 2022; Accepted 1 November 2022
Available online 5 November 2022

by the strong vapor plume ejected by the melt pool [6]. Ammer et al. developed a model for the Selective Electron Beam Melting process (SEBM), which accounts for the specificity of the electron beam absorption compared to that of laser [7]. Gürtler et al. presented an implementation based on the Volume of Fluid (VoF) method using the open-source code OpenFOAM [8]. Use of the finite element framework together with a level set method to resolve phase domains was recently applied to compute melt pool sizes for the IN738 alloy, where good agreement was found with measurements across a wide process window [9]. With specific focus on the powder sintering and consolidation process, Wang et al. developed a phase field implementation [10] which elucidates the process of powder necking.

Modeling of microstructure evolution is of equal importance [11]. Early work by Lu et al. [12] used the phase field method to study microstructure evolution in two-dimensional cross-sections. Liu et al. [13,14] recently discussed solidification phenomena focusing on dendrite growth and grain formation using combined phase-field and Lattice-Boltzmann methods, also in two-dimensional crosssection. Significant efforts are ongoing by the "ExaAM" program by Turner et al. [15], which is demonstrating three-dimensional microstructure evolution for additive manufacturing components at *exa* computing scale. As a computational method, Cellular Automata (CA) has emerged as a powerful tool to solve for grain nucleation and growth following the thermal gradients typical for AM processes, and has been applied to SEBM [16], Directed Energy Deposition (DED) [17]. For single tracks, Shi et al. demonstrated the coupling between CA and arbitrary Lagrangian–Eulerian (ALE) framework and applied it to Ti6Al4V [18], while extension of the method to multiple scan vectors and layers was recently demonstrated by Yang et al. where the phase transition was modeled using the phase field method [19]. Taken together, this significant body of work illustrates the recent advances in state of the art modeling and simulations for additive manufacturing while also highlights the open challenges that still separate us from a full digitalization of L-PBF AM.

To convincingly reach this goal, an important milestone is the capability to model melt pool dynamics, porosity, microstructure, and multiple scan vectors and layers concurrently to reach a domain size comparable to experiments. Such capability needs to be able to systematically explore the role of process parameters in determining part quality as concurrently measured by part density (defects) and microstructure features (grains size and shape), which is still lacking in the literature. In this work, we present our coupled three-dimensional computational framework where we co-evolve the thermal field, solid–liquid phase transformations, porosity and microstructure at the same time. Our approach is based on the phase field method and is coupled to LBM solver to model the melt pool. We implement the model in parallel message passing interface (MPI) communication and we validate it in terms of predicted porosity and microstructure choosing the INCONEL 718 super-alloy as material system. Next, we apply the model to quantitatively explore how microstructure and porosity respond to process parameters, explicitly in three dimensions. The framework exposes multiple scan tracks within a layer, and build multiple layers to ultimately produce a domain of cubic shape at millimeter size. Such domain is thus a representative volume element (RVE) of the built component, which further serves as an important component in full multi-scale simulations of L-PBF.

2. Method

2.1. Phase field model

The phase-field method applied in this work describes the evolution of the multidimensional order parameter $\overline{\phi}$:

$$\overline{\phi} = \left[\phi_l, \phi_v, \phi_{g_1} \ldots, \phi_{g_N}\right]. \tag{1}$$

The components of $\overline{\phi}$ account for vacuum, liquid and grains of the microstructure. The number of allowed grain orientations (grain order parameters) needs to be large, and is set to 10^4 in this work. The presence of the vacuum order parameter allows our model to utilize a diffuse interface approach, which simplifies integration with the fluid dynamics solver. $\overline{\phi}$ evolves by minimizing the free energy of the system

$$F = \int \left[W g + \frac{K}{2} \sum_i \left(\nabla \phi_i\right)^2 + f_\rho + f_{tr} \right] dV. \tag{2}$$

The bulk component of the free energy density g is defined following formulation proposed by Moelans et al. [20–22],

$$g = \sum_i \left(\frac{\phi_i^4}{4} - \frac{\phi_i^2}{2} \right) + \frac{3}{2} \sum_{i<j} \phi_i^2 \phi_j^2 + \frac{1}{4} \tag{3}$$

The second term in Eq. (2) introduces the interface contribution to the free energy. The parameters W and K are interface-selective and are computed following Moelans et al. formulation:

$$W = \frac{\sum_{i<j} W_{ij} \phi_i^2 \phi_j^2}{\sum_{i<j} \phi_i^2 \phi_j^2} \tag{4}$$

$$K = \frac{\sum_{i<j} K_{ij} \phi_i^2 \phi_j^2}{\sum_{i<j} \phi_i^2 \phi_j^2}, \tag{5}$$

where $W_{ij} = \frac{3\sigma_{ij}}{4\Delta}$ and $K_{ij} = 6\sigma_{ij}\Delta$. σ_{ij}, and Δ are the interfacial energies and the interfacial width. The third term in Eq. (2) is introduced to enforce mass conservation:

$$f_\rho = \frac{1}{2} C_\rho \left[\rho - \left(h_l + \sum_g h_g \right) \right]^2, \tag{6}$$

where the coupling constant C_ρ is an adjustable parameter, ρ is an independent order parameter, h_l and h_g are the liquid and grains phase fractions defined within Moelans model:

$$h_i = \frac{\phi_i^2}{\sum_i \phi_i^2}. \tag{7}$$

The final term in Eq. (2) is introduced to drive the solid–liquid phase transition:

$$f_{tr} = \sum_i G_i h_i, \tag{8}$$

where G_i is the free energy of a particular phase. A detailed discussion concerning this term is presented in the next section.

The components of $\overline{\phi}$ evolve as non-conserved fields,

$$\frac{\partial \phi_i}{\partial t} = -\Gamma \mu_i - \mathbf{u} \cdot \nabla \phi_i, \tag{9}$$

while ρ evolves as a conserved field,

$$\frac{\partial \rho}{\partial t} = \Gamma_\rho \nabla^2 \mu_\rho - \mathbf{u} \cdot \nabla \rho, \tag{10}$$

where $\mu_i = \frac{\partial F}{\partial \phi_i}$ and $\mu_\rho = \frac{\partial F}{\partial \rho}$. The convection velocity $\mathbf{u}$ in the advection terms in Eqs. (9) and (10) is provided by the fluid dynamics solver discussed in Section 2.5. Γ_ρ is a material independent parameter, chosen to ensure mass conservation during simulation. Γ determines the rate of solid–liquid transition, similarly to W and K, it is interface sensitive:

$$\Gamma = \frac{\sum_{i<j} \Gamma_{ij} \phi_i^2 \phi_j^2}{\sum_{i<j} \phi_i^2 \phi_j^2}, \tag{11}$$

where Γ_{ij} is the ij interface mobility. The evolution equations are solved using regular grid under periodic boundary conditions in horizontal directions, and zero flux condition in the vertical direction. Simple explicit finite difference method is used for time propagation.

Grain growth anisotropy is introduced using orientation-dependent grain/liquid interfacial mobility [23,24]

$$\tilde{\Gamma}_{lg} = \Gamma_{lg} (1 - 3\delta) \left[1 + \frac{4\delta}{1 - 3\delta} \left\{ \left(n_x'\right)^4 + \left(n_y'\right)^4 + \left(n_z'\right)^4 \right\} \right], \tag{12}$$

where δ is an anisotropy parameter, $\mathbf{n}' = \mathbf{Rn}$, where $\mathbf{n} = \nabla\phi_g/|\nabla\phi_g|$ is normal direction to the grain/liquid interface, $\mathbf{R}$ is the rotation matrix from global to local frame constructed in the following way:

$$\mathbf{R} = \mathbf{BCD} \tag{13}$$

$$\mathbf{D} = \begin{bmatrix} \cos\alpha & \sin\alpha & 0 \\ -\sin\alpha & \cos\alpha & 0 \\ 0 & 0 & 1 \end{bmatrix}$$

$$\mathbf{C} = \begin{bmatrix} 1 & 0 & 1 \\ 0 & \cos\beta & \sin\beta \\ 0 & -\sin\beta & \cos\beta \end{bmatrix}$$

$$\mathbf{B} = \begin{bmatrix} \cos\gamma & \sin\gamma & 0 \\ -\sin\gamma & \cos\gamma & 0 \\ 0 & 0 & 1 \end{bmatrix}$$

where polar angles defining grain orientation are $\alpha = 2\pi x$, $\beta = \arccos(2y-1)$, $\gamma = 2\pi z$, with x, y, z randomly generated from $[0, 1]$.

2.2. Solid–liquid phase transition

In order to incorporate a driving force for solid–liquid transition, we rewrite Eq. (9)

$$\frac{\partial\phi_i}{\partial t} = -\Gamma\left(\mu_i^d + \mu_i^m\right), \tag{14}$$

where μ^m and μ^d are the melting and diffusive part of the potential, defined in the following way:

$$\mu_i^m = \frac{\partial f_{tr}}{\partial\phi_i} = \sum_j G_j(T)\frac{\partial h_j}{\partial\phi_i} \tag{15}$$

$$\mu_i^d = \mu_i - \mu_i^m$$

where $G_j(T)$ are the temperature-dependent Gibbs free energy of phase j. In the following we assume no driving force for transition at grain/vacuum, grain/grain and liquid/vacuum interfaces, therefore,

$$\begin{aligned} G_g &= G_v \\ G_l &= G_v \\ G_g &= G_g' = 0 \end{aligned} \tag{16}$$

The values of the Gibbs free energy at grains were taken as reference and set to zero. Formally, the formulation in Eq. (16) introduces a jump in free energy in the bulk of the vacuum region, without practical consequence. Including this into Eq. (15) allows to relate μ_g^m and μ_l^m only to the Gibbs free energy of the liquid phase G_l,

$$\mu_g^m = G_l\frac{\partial h_l}{\partial\phi_g} \tag{17}$$

$$\mu_l^m = G_l\left(\frac{\partial h_v}{\partial\phi_l} + \frac{\partial h_l}{\partial\phi_l}\right). \tag{18}$$

where G_l is related to the latent heat of fusion L and the melting temperature T_m

$$G_l = -\frac{L}{T_m}\left(T - T_m\right). \tag{19}$$

2.3. Nucleation

Within our phase-field formulation, phase transition between solid and liquid needs to be initiated by the nucleation. The transition from solid to liquid phase at $T > T_m$ does not affect the grain structure and is modeled using simple formulation for nucleation flux j_l

$$j_l(\Delta T) = -j_g(\Delta T) = \left[N_s\left(h_v h_g\right) + N_b\right]\eta(\Delta T), \tag{20}$$

where j_l and j_g are the phase fluxes, $\Delta T = T - T_m$, and $\eta(\Delta T)$ is a cutoff function ($\eta(\Delta T) = 0$ for $T < T_m$ and $\eta(\Delta T) = \Delta T$ for $T > T_m$). N_s and N_b are small constants ($10^{-4} - 10^{-5}$ in adimensional units) controlling the strength of the nucleation flux at the solid/vacuum interface and bulk. On the other hand, the details of grain nucleation from the liquid phase at $T < T_m$ can affect the final grain micro-structure. Therefore an approach offering more control is adopted in this work [25,26], with the nucleation flux defined as

$$\begin{aligned} j_g(\Delta T) &= -j_l(\Delta T) \\ &= \frac{j_{max}}{\sqrt{2\pi}\Delta T_\sigma}\int_0^{\Delta T}\exp\left(-\frac{1}{2}\left(\frac{\Delta T - \Delta T_N}{\Delta T_\sigma}\right)^2\right)d(\Delta T). \end{aligned} \tag{21}$$

The average under-cooling temperature ΔT_N and its standard deviation ΔT_σ are the input parameters, while j_{max} is proportional to density of nucleation centers.

2.4. Thermal solver

The temperature field is computed solving the standard heat diffusion equation within the region of the RVE occupied by the solid and liquid phases. Periodic boundary conditions in the lateral directions are applied. At the bottom boundary of the RVE and at the solid/vacuum and liquid/vacuum interfaces (which is the top surface of the printed material), the second derivative of temperature in the vertical direction is set to zero. The heat equation is

$$\boldsymbol{\nabla}\cdot\kappa\boldsymbol{\nabla}T + \rho c_p\boldsymbol{\nabla}T\cdot\mathbf{u} + \dot{q} = \rho c_p\frac{\partial T}{\partial t}, \tag{22}$$

where ρ, κ and c_p are the material density, heat conductivity and heat capacity, respectively. The second term describes effects of convective flow, and $\dot{q}$ represents the various source terms

$$\dot{q} = \dot{q}_l + \dot{q}_c + \dot{q}_r + \dot{q}_v + \dot{q}_f. \tag{23}$$

The term $\dot{q}_l$ represents the heat source due to the laser beam. In principle, it is possible to model the laser beam explicitly by ray tracing, including the reflections and interaction with the material/powder surface [27,28]. However, in order to lower the computational cost of the modeling approach, a simplified model is applied in which the heat source assumes a Gaussian shape [27,29]

$$\dot{q}_l = AP_L\left[\frac{1}{2\pi R_L^2}\exp\left(-\frac{r^2}{2R_L^2}\right)\right]\left[\left(1-h_v\right)\frac{1}{D_L\sqrt{2\pi}}\exp\left(-\frac{d^2}{2D_L^2}\right)\right], \tag{24}$$

where A and P_L are the laser absorptivity and power. The parameters R_l and D_L are the beam radius and penetration depth. r is the distance from the center axis of the laser beam and d is the penetration depth measured from the top surface of the material or melt pool. The factor $\left(1-h_v\right)$ limits the overall absorptivity relative to the content of vacuum phase fraction (h_v). $\dot{q}_c$ in Eq. (23) represents the convection term used to model the heat transfer from the RVE to the rest of the part through the bottom of the RVE and convection due to chamber atmosphere applied at the interface with vacuum,

$$\dot{q}_c = -\eta C_b\left(T - T_b\right), \tag{25}$$

where C_b is a convection coefficient and T_b is a temperature of the material surrounding the RVE. $\eta = |\nabla h_v|$ is an interface function allowing to capture the effect of the diffuse interface. $\dot{q}_r$ represents radiation cooling

$$\dot{q}_r = -\eta C_r\sigma\left(T^4 - T_b^4\right), \tag{26}$$

where C_r is the black-body constant. $\dot{q}_v$ captures vaporization cooling,

$$\dot{q}_v = -\eta C_v\frac{1}{\sqrt{2\pi R_g T}}p_r L_v\exp\left(\frac{L_v}{R_g}\left(\frac{1}{T_v} - \frac{1}{T}\right)\right), \tag{27}$$

where p_r is the reference pressure, R_g is the gas constant, T_v is the vaporization temperature, L_v is the latent heat of vaporization, and C_v is an adjustable constant. The large value of L_v may cause fluctuations of temperature around T_v, in order to avoid this, $\dot{q}_v$ term is not allowed

to decrease temperature below T_v. $\dot{q}_f$ is contribution from the latent heat of fusion due to the solid/liquid transformation,

$$\dot{q}_f = \left.\frac{\partial h_l}{\partial t}\right|_{g\leftrightarrow l} L_f, \tag{28}$$

where h_l is liquid phase fraction and L_f is the latent heat of fusion. Similar to vaporization cooling, temperature change due to this term is not allowed to cross melting temperature, limiting the value of phase change flux.

2.5. Melt pool dynamics

Melt pool flow solver delivering velocity ($\mathbf{u}$) to advection term in evolution equations is implemented in the Lattice Boltzmann Method (LBM) [30] framework. Our implementation follows the formalism developed for incompressible flow by Guo et al. [31]. The evolution equation of the distribution function in BGK approximation reads

$$f_\alpha\left(\mathbf{x}+\mathbf{e}_\alpha, t+1\right) = f_\alpha\left(\mathbf{x},t\right) - \frac{f_\alpha - f_\alpha^{eq}}{\tau+1/2} + F_\alpha\left(\mathbf{x},t\right), \tag{29}$$

where the time step and grid spacing were set to 1. $\tau = \nu/c_s^2\Delta t$ is the relaxation time, and f^{eq} is the equilibrium distribution function

$$f_\alpha^{eq} = \begin{cases} -\left(1-\omega_0\right) - \omega_0\frac{u^2}{2c_s^2}, & \alpha = 0 \\ \omega_\alpha\left[\frac{p}{c_s^2} + \frac{\mathbf{e}_\alpha\cdot\mathbf{u}}{c_s^2} + \frac{\left(\mathbf{e}_\alpha\cdot\mathbf{u}\right)^2}{c_s^4} + \frac{u^2}{2c_s^2}\right]. & \alpha \neq 0 \end{cases} \tag{30}$$

In this work d3q15 (d-stands for dimensionality, q-size of the velocity set) velocity $\mathbf{e}_\alpha$ set has been applied

$$\mathbf{e} = \begin{bmatrix} 0 & 1 & 0 & 0 & -1 & 0 & 0 & 1 & -1 & 1 & 1 & -1 & 1 & -1 & -1 \\ 0 & 0 & 1 & 0 & 0 & -1 & 0 & 1 & 1 & -1 & 1 & -1 & -1 & 1 & -1 \\ 0 & 0 & 0 & 1 & 0 & 0 & -1 & 1 & 1 & 1 & -1 & -1 & -1 & -1 & 1 \end{bmatrix} \tag{31}$$

with the weight coefficients

$$\omega_\alpha = \begin{cases} 2/9 & \alpha = 0 \\ 1/9 & \alpha = 1,\ldots,6 \\ 1/72 & \alpha = 7,\ldots,14. \end{cases} \tag{32}$$

The forcing term $F_\alpha\left(\mathbf{x},t\right)$ reads

$$F_\alpha = \frac{\tau}{\tau+1/2}\omega_\alpha\left(\mathbf{e}_\alpha/c_s^2\right)\cdot\mathbf{F}/\rho \tag{33}$$

and accounts for the effect of surface tension ($\mathbf{F}_s$), recoil pressure ($\mathbf{F}_r$), Marangoni ($\mathbf{F}_M$) force and gravity ($\mathbf{F}_g$) .

$$\mathbf{F} = \mathbf{F}_s + \mathbf{F}_r + \mathbf{F}_M + \mathbf{F}_g \tag{34}$$

In order to integrate the LBM formalism with the phase field model an auxiliary phase ϕ is introduced

$$\phi = h_l + \sum_g h_g \tag{35}$$

where h_l and h_g are the liquid and grain phase fractions evaluated using formula in Eq. (7). The surface tension force is expressed in the potential form [32,33]

$$\mathbf{F}_s = \mu_{LBM}\nabla\phi, \tag{36}$$

where the potential μ_{LBM} is evaluated using the double-well auxiliary free energy [34,35]

$$\mu_{LBM} = 4\beta\left[\phi\left(\phi-1\right)\left(\phi-1/2\right)\right] - \kappa\nabla^2\phi. \tag{37}$$

$\beta = 12\sigma/\xi$, and $\kappa = 3\sigma\xi/2$, where σ is surface tension, ξ is the interfacial thickness set to $\xi = \Delta/2$. The different definition of the free energy model in our LBM implementation and the phase field model may result in spurious forces at the liquid/vacuum interface. The effect can be reduced enforcing equilibrium $\mu_{LBM} = 0$ for interface with zero curvature, such that the interface profile is controlled by phase-field solver and curvature by LBM solver. The modified formula for μ_{LBM} follows

$$\mu_{LBM} = -\kappa\left[\nabla^2\phi - \left(\mathbf{n}\cdot\boldsymbol{\nabla}\right)\left(\mathbf{n}\cdot\boldsymbol{\nabla}\right)\phi\right], \tag{38}$$

where $\mathbf{n} = \nabla\phi/\left|\nabla\phi\right|$ is the vector normal to the interface. The force components due to gravity, recoil pressure and Marangoni effect are defined as follows

$$\mathbf{F}_g = -h_l g\hat{z} \tag{39}$$

$$\mathbf{F}_r = p_r\exp\left[\frac{L_v}{R_g}\left(\frac{1}{T_v} - \frac{1}{T}\right)\right] \tag{40}$$

$$\mathbf{F}_M = C_M\left[\nabla T - \left(\mathbf{n}\cdot\nabla T\right)\mathbf{n}\right], \tag{41}$$

where C_M is the Marangoni constant, p_r is the recoil reference pressure, L_v is the vaporization latent heat and T_v is the boiling temperature.

The LBM solver is active within the melt pool domain, determined by condition

$$h_l > L_l \tag{42}$$

where L_l is the minimal amount of liquid fraction, set to 10^{-3}. Considering boundary conditions on the vacuum side, the missing components of the distribution functions are reconstructed using a simple anti-bounce-back scheme commonly used to model flow with free surface [36,37] in the context of the "volume of fluid" method

$$\tilde{f}_\alpha\left(\mathbf{x}-\mathbf{e}_\alpha,t\right) = f_\alpha^{eq}\left(\rho_G,\mathbf{u}\right) + f_{\bar{\alpha}}^{eq}\left(\rho_G,\mathbf{u}\right) - f_{\bar{\alpha}}\left(\mathbf{x},t\right), \tag{43}$$

where $\tilde{f}_\alpha$ represents the distribution function after the collision step and before the propagation step. ρ_G is the gas density related to chamber pressure $p_G = \rho_G/3$, which can be an input parameter, and is taken as $p_G = 0$ in our calculations. On the solid side of the boundary, a simple bounce-back method [38,39] is used to reconstruct the unknown distribution function incoming from the solid side of the melt-pool boundary

$$\tilde{f}_\alpha\left(\mathbf{x}-\mathbf{e}_\alpha,t\right) = f_{\bar{\alpha}}^{eq}\left(\mathbf{x},\mathbf{u}_s\right) + f_{\bar{\alpha}}^{eq}\left(\mathbf{x},\mathbf{u}_s\right) - f_{\bar{\alpha}}\left(\mathbf{x},t\right). \tag{44}$$

Alongside the bounce-back scheme, the immersed boundary conditions are implemented as proposed by Noble and Torczynski [40] and modified by Strack and Cook [41]. Following this scheme, Eq. (29) is modified

$$f_\alpha\left(\mathbf{x}+\mathbf{e}_\alpha,t+\delta t\right) = f_\alpha\left(\mathbf{x},t\right) + \left(\Omega_\alpha\left(\mathbf{x},t\right) + F_\alpha\left(\mathbf{x},t\right)\right)\left(1-B\right) + \Omega_\alpha^S B, \tag{45}$$

where the parameter B is a function of the solid phase fraction

$$B = \frac{\left(\sum_g h_g\right)\tau}{\left(1-\sum_g h_g\right)+\tau}, \tag{46}$$

Collision operator Ω_α^S defined after Noble and Torczynski,

$$\Omega_\alpha^S = f_{\bar{\alpha}} - f_{\bar{\alpha}}^{eq} + f_\alpha^{eq}\left(\mathbf{u}_s\right) - f_\alpha. \tag{47}$$

Two-relaxation time (TRT) approximation offers improved numerical stability [42–44] comparing to single-relaxation scheme without losing computational efficiency. TRT approximation propagates the distribution functions using positive and negative linear combinations of Eq. (29), leading to separate equations for f_α^+ and f_α^- with equilibrium functions f_α^{eq+} and f_α^{eq-}

$$\begin{aligned} f_\alpha^+ &= \left(f_\alpha + f_{\bar{\alpha}}\right)/2, & f_\alpha^- &= \left(f_\alpha - f_{\bar{\alpha}}\right)/2 \\ f_\alpha^{eq+} &= \left(f_\alpha^{eq} + f_{\bar{\alpha}}^{eq}\right)/2, & f_\alpha^{eq-} &= \left(f_\alpha^{eq} - f_{\bar{\alpha}}^{eq}\right)/2. \end{aligned} \tag{48}$$

and f_α^+ is propagated with τ^+, f_α^- is propagated with τ^-,

$$\tau^+ = \tau = \nu/c_s^2\Delta t \tag{49}$$

$$\tau^- = \Lambda/\tau^+\Delta t^2 \tag{50}$$

where $\Lambda = 1/4$.

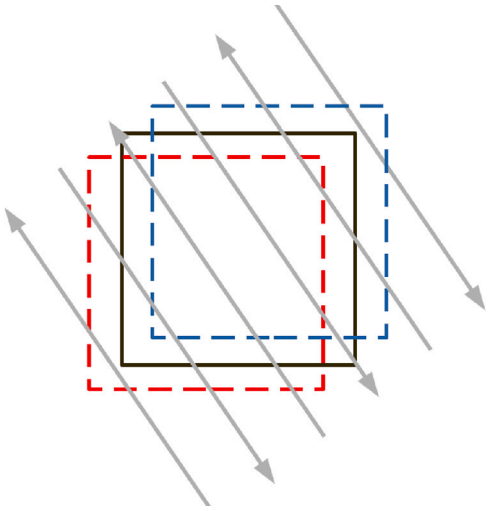

Fig. 1. The number of scan lines (gray arrows) crossing the RVE depends on the relative position of the RVE with respect to the scan path. Three different choices are represented with squares of different colors.

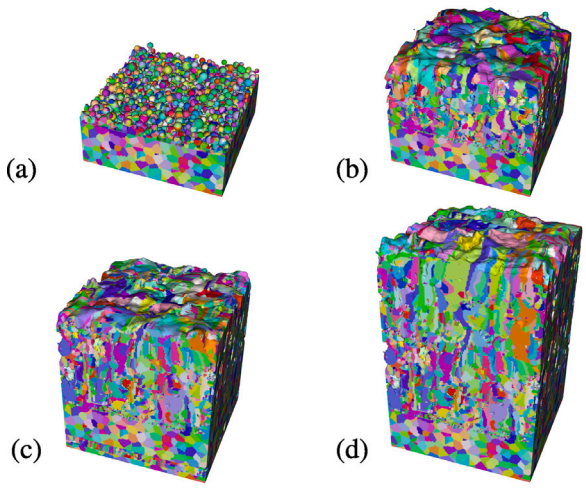

Fig. 2. Progression of the three-dimensional simulation building a cube of material by selective laser melting. Snapshots in time report the simulation (a) at the initial condition; (b) after the completion of the seventh layer; (c) after the completion of the twelveth layer; and (d) at the completion of the eighteenth layer.

3. Implementation details, model and material parameters

Material (Nickel superalloy INCONEL 718) and model parameters are collected in Table 1. The implementation follows the explicit scheme with time step $\Delta t = 5 \times 10^{-8}$ s and uniform grid with spacing $\Delta x = 5 \times 10^{-6}$ m. Initial substrate width is set to 50 grid points (0.25 mm), vacuum width is set to 50 mesh points, which results in total RVE height of 100 grid points (0.5 mm). The powder is distributed using a rain drop algorithm in which the particles are seeded at random positions and allowed to fall into a local minima on the prior surface one after another. The technical information of the powder such as particle size, shape, and composition are available in Q. B. Nguyen et al. [45]. The particles radii follow a binormal distribution with peak at 25.5×10^{-6} m and square root of left and right variances of $\sigma_L = 2 \times 10^{-6}$ m and $\sigma_R = 10^{-5}$ m. Eighteen (18) layers of powder are deposited in order to build a cube, each layer corresponding to 40×10^{-6} m of material. The height of the RVE is kept constant during build by removing an equivalent layer thickness from the bottom of the domain each time a new layer of powder is added to the top surface. After the simulation is complete, all layers are reassembled for post processing.

Each layer consists of parallel scan lines, separated by hatch spacing, such that adjacent lines follow opposite directions. In our simulations, we assumed that, for each scan vector, the laser travels for a sufficient time for our RVE to cool down to boundary temperature T_b. The scan lines in each subsequent layer are rotated by 67° relative to the previous one. Most often hatch spacing is not commensurate with RVE geometry and the number of scan lines crossing RVE (only those are included in the calculations) depends on the position of the RVE, this situation is presented in Fig. 1. Therefore centering of the layer is randomized in the direction perpendicular to the line direction. This ensures correct average number of lines crossing the RVE, counting multiple layers.

The progression of the layer-by-layer simulation is shown in Fig. 2 for the representative case of default process parameters, i.e., laser power of 285 W, scan speed of 0.96 m/s, and hatch spacing of 0.11 mm, corresponding to the EOS infill inskin parameters for INCONEL 718. From the computational domain, rendering was done using The Visualization Toolkit (VTK) with in-house code where the microstructure was resolved according to grain orientation in a digital EBSD map. As material is deposited on top of the substrate, within 1 layer thickness the microstructure undergoes transition from the coarse, equiaxed of the substrate to a finer, columnar microstructure of the solidified metal. Such feature confirms the observations of Yang et al. [19].

Numerical implementation used multi-processor architecture through Message Passing Interface (MPI) and Cartesian communicator. The calculations were performed on a computational cluster using 8×24 Intel Xeon E5-2690 v3 @ 2.6 GHz processors. The run time to simulate 18 layers depends on the process parameters (hatch spacing and laser speed), however for the "optimal" scan parameters (see Fig. 2), it is close to 24 h.

4. Samples manufacturing and testing

Selective Laser Melting (SLM) was used to manufacture cylindrical samples using an EOS M290 printer (EOS GmbH, Krailling, Germany). The dimensions of the samples were 40 mm in length and 7 mm in diameter with extra 0.75–1 mm height as allowance for the subsequent wire cut process. The role of process parameters was studied by varying laser power, laser scan speed and hatch spacing across three values each, with their default ("optimized") value and ±25% of the optimized value. For each combination of process parameters, two series of samples were printed, one where the cylinder was oriented along the build direction, and the other where it was oriented perpendicular to the build direction, i.e., along the base plate direction. The values of these parameters are shown in Table 2. Layer thickness was kept at 0.04 mm. The printing process was performed with bed heating temperature at 80 °C, laser spot size in 100 μm, laser wavelength at 1060 nm–1100 nm. The direction of laser scan was rotated 67°after each layer with infill inskin theme followed by contour.

The different values process parameters and sample orientations resulted in a total of 56 different combinations. Five sample replicas were fabricated for each parameter combination, resulting in a total of 280 samples. After print, the samples were separated from the build plate by EDM wire cut. To remove dirt before further characterization, ultrasonic bath for five minutes and followed by air gun drying was used.

The relative density for porosity estimation was determined using Archimedes principle, using an analytical balance (KERN ALJ) together with a density measuring kit. Two separate measurements were taken from each of the 5 replicas with a given combination of process parameters and orientation. Ten measurements were done for each sample and their mean and standard deviation are plotted in Fig. 5. The assumptions used in the calculation of relative density were that

Table 1
Material and model parameters for INCONEL 718.

Thermal solver			
Property	Symbol	Units	Value
Material density [46]	ρ	kg/m^3	8220
Specific heat [47]	c_p	J/kgK	440
Heat conductivity [47]	κ	W/mK	60
Cooling factor bottom	C_b	–	10^{-5}
Convection heat transfer coefficient	C_t	Wm^{2}K	50
Surface evaporation coefficient	C_v	–	10
Absorptivity	A	–	0.7
Heat source radius	R_L	m^{-6}	37.5
Heat source penetration depth	D_L	m^{-6}	20
Latent heat vaporization [48]	L_v	J/kg	5.49×10^6
Latent heat formation [47]	L_f	J/kg	2.819×10^3
Melting temperature [46]	T_v	K	1533.15
Boiling temperature [46]	T_m	K	3174
Phase solver			
Interfacial energy (solid/liquid)	σ_{lg}	N/m	0.17
Interfacial width	Δ	m^{-6}	10
Interfacial mobility (solid/vacuum)	Γ_{gv}	m^3/sJ	10^{-4}
Interfacial mobility (liquid liquid/vacuum)	Γ_{lv}	m^3/sJ	10^{-4}
Interfacial mobility (liquid liquid/solid)	Γ_{lg}	m^3/sJ	10^{-5}–10^{-3}
Grain anisotropy parameter	δ	–	0.2
Strength of phase/density coupling	C_ρ	–	10
Interfacial mobility (density)	Γ_ρ	–	10^{-4}
Nucleation undercooling (grain)	ΔT_N	K	20
Nucleation undercooling standard deviation (grain)	ΔT_σ	K	8
Nucleation flux (liquid, grain bulk)	N_b	1/Km^{3}s	10^{20}
Nucleation flux (liquid, grain/vacuum)	N_s	1/Km^{3}s	10^{19}
LBM			
Viscosity [49]	ν	Pa s	$7.5 \cdot 10^{-4}$
Surface tension [49]	σ	N/m	1.7
Interfacial width	Δ	m^{-6}	5
Marangoni force coefficient [49]	C_M	N/mK	$-2.8147 \cdot 10^{-4}$
Recoil reference pressure [49]	p_r	Pa	$5.371 \cdot 10^4$

Table 2
Specification and variations of process parameters.

Process parameters	Specification and variations
Laser power	Optimized value and ±25% of the optimized value (285 W, 356.25 W, 213.75 W)
Laser scan speed	Optimized value and ±25% of the optimized value (960 mm/s, 1200 mm/s, 720 mm/s)
Hatch spacing	Optimized value and ±25% of the optimized value (0.11 mm, 0.14 mm, 0.08 mm)
Build orientation	x/y and z direction
Scan strategy	Stripe strategy

the density of water is 1.000 g/cm^3 and that the density of fully-dense INCONEL 718 is 8.22 g/cm^3.

EBSD analysis was performed by setting the threshold for grain identification to 10 pixels per grain, which corresponded to a minimum grain diameter of 8.92 μm, using a step size of 2.5 μm. The typical number of grains in each EBSD map was 2000. Maps were colored such that the build direction was the (001) direction ("IPF-z" convention). EBSD maps along the horizontal direction (later referred to "XY") were extracted from the samples printed in the horizontal direction, while EBSD maps along the vertical direction ("XZ") were extracted from the vertical samples.

5. Model calibration

Most of the parameters listed in Table 1 are known material constants for INCONEL 718. However, few of them are adjustable model parameters. In our experience, one of the key parameters is the evaporation coefficient C_v which controls the efficiency of evaporation cooling, and greatly affects the recoil pressure and the shape of the melt pool. The effect of this parameter is presented in Fig. 3. As expected, smaller values of C_v result in higher maximum temperature of the melt pool (well above the vaporization temperature T_v) and results in violent recoil effect. For instance, using $C_v = 2$, we observed the melt pool splashing material over the neighboring powder particles, while the value of $C_v = 10$ leads to a more regular shape of the melt pool (Fig. 3a). This effect translates to the surface roughness of the solidified layer, such that trails of the scan track are clearly visible for low C_v, while the surface roughness is lower for larger C_v. The strength of the recoil pressure depends directly on the laser power, comparison between 200 W and 300 W is shown in Fig. 3b. The value of C_v can be adjusted according to the expected shape of the solidified layer and melt pool shape. Further results are produced with value of $C_v = 10$.

A key parameter that affects the grain structure is the interfacial mobility at liquid/grain interface (Γ_{gl}). The value of Γ_{gl} directly controls the rate of solid–liquid transition, and through that affinity to liquid undercooling or solid overheating. The extent of melt pool undercooling determines the rate of grain nucleation, directly affecting the resulting grain structure. The effect is summarized in Fig. 4a. Clearly, smaller values of $\Gamma_{gl} = 10^{-5}$ result in much finer and equiaxed grains compared to the result derived from a larger mobility of $\Gamma_{gl} = 10^{-3}$. Smaller mobility allows for larger undercooling creating conditions for nucleation in front of the interface. To simplify the presentation, the parametrization of the nucleation model was kept fixed at the values listed in Table 1 and setting T_b to 600 K, and process parameters to their "optimal" values.

It seems possible, that the value of Γ_{gl} can by calibrated by comparing the simulated grain structure (for instance, size and aspect ratio distributions) with their experimental counterparts. The comparison between computed and measured properties of cross-sections in the "XZ" plane are presented in Fig. 4b. The corresponding EBSD map for experimentally printed sample is shown in Fig. 4c. In order to compute the distributions, the computational domain is analyzed in slice by slice

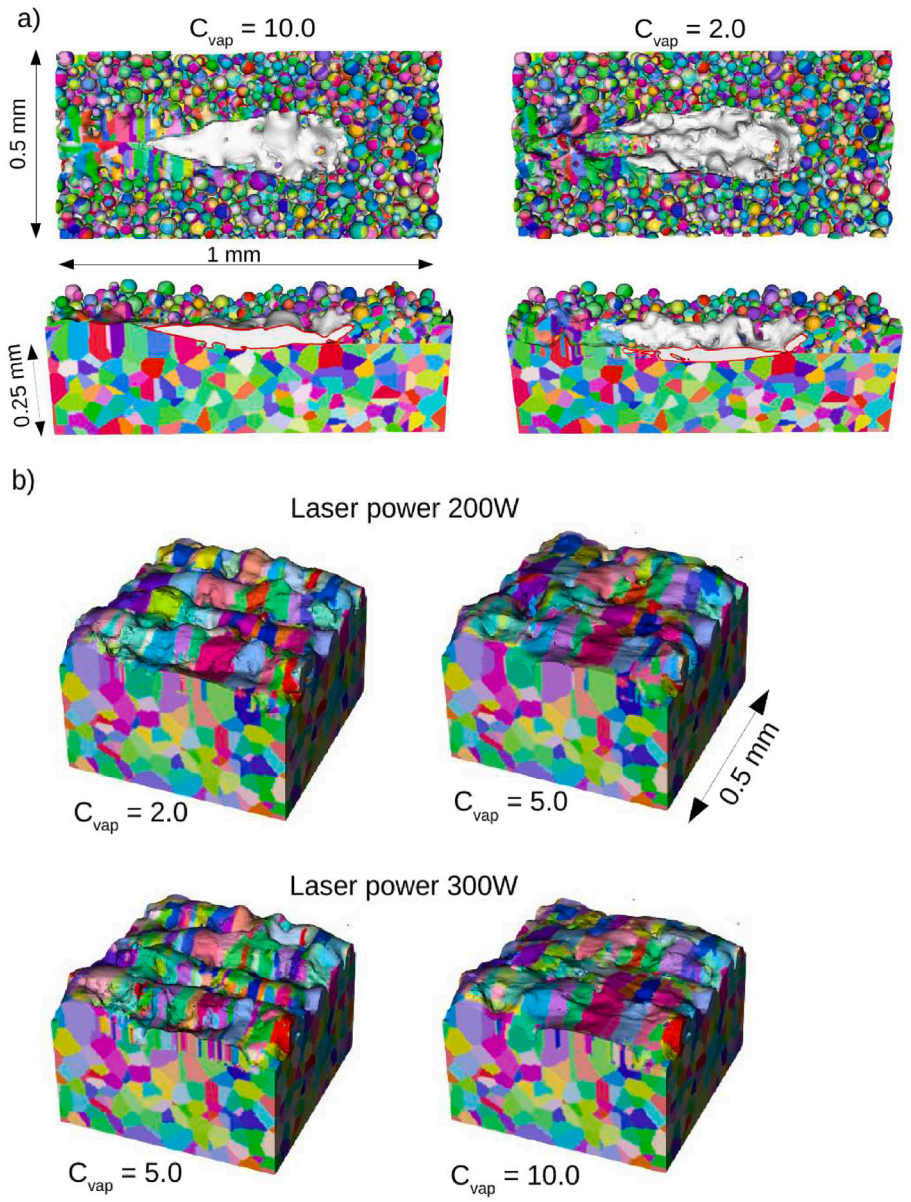

Fig. 3. (a) Melt-pool shape computed at laser power 250 W and laser speed 1 m/s, for vaporization cooling factor C_v equal 2 and 10. (b) shape of the solidified layer after laser scan completion for laser power 200 W and 300 W and two values of surface evaporation coefficient C_v.

manner and average over whole RVE. The distributions peak at low values of grain size or aspect ratio, and then decrease exponentially for large values. Despite clearly different grain structures, the distributions seem not to depend strongly on the values of Γ_{gl}, and at the same time they quite well agree with the experimentally observed ones. Comparing EBSD maps from Fig. 4a and c it seems reasonable take the value of $\Gamma_{gl} = 5 \times 10^{-5}$ for the remaining part of this paper.

6. Results and discussion

The framework presented in the previous section was used to systematically build digital cubes at different process parameters. Each cube was then post-processed to extract porosity and characterize microstructure. Porosity was computed as the fraction of empty volume (vacuum phase fraction is $h_v > 0.5$) relative to the portion of RVE excluding the top surface as well as the substrate to ensure the calculation is representative only of the actual material built. Because the heat source enters and leaves the RVE at its lateral sides, the sides of the cube are not considered representative and they are also excluded from the porosity calculation. Computed values for different combinations of process parameters are compiled in Fig. 5. The process parameters are encoded as a sequence of three symbols "LSH" representing laser power, scan speed and hatch spacing, where "0" stands for the optimal values, while "+ " and "-" indicate increase and decrease by 25% relative to the optimal value. The optimal values are 285 W for laser power, 960 mm/s for laser speed and 0.11 mm for hatch spacing. Inspection of Fig. 5 reveals a number of interesting features of the L-BPF process. First, we note that porosity remains relatively stable, with deviations from full density never larger than 2.2%. To put this result in perspective, we recall that the line energy density, defined by $d = \frac{P}{vhh}$ where h is the layer thickness (40 μm in our modeling and experiments), is generally a useful proxy to part quality. Calculation of d gives $d = 67.4$ J/mm^3 for print "OOO", while $d = 31.8$ J/mm^3 for "-++" with a maximum of $d = 154.6$ J/mm^3 for "+–"", showing a range as large as 170% of the "OOO" value. At the same time, the combination "-++" shows statistically significant increase in porosity. Here, a reduction in laser power coupled to an increase in scan speed reduces the melt pool cross-section area, thus limiting the ability of

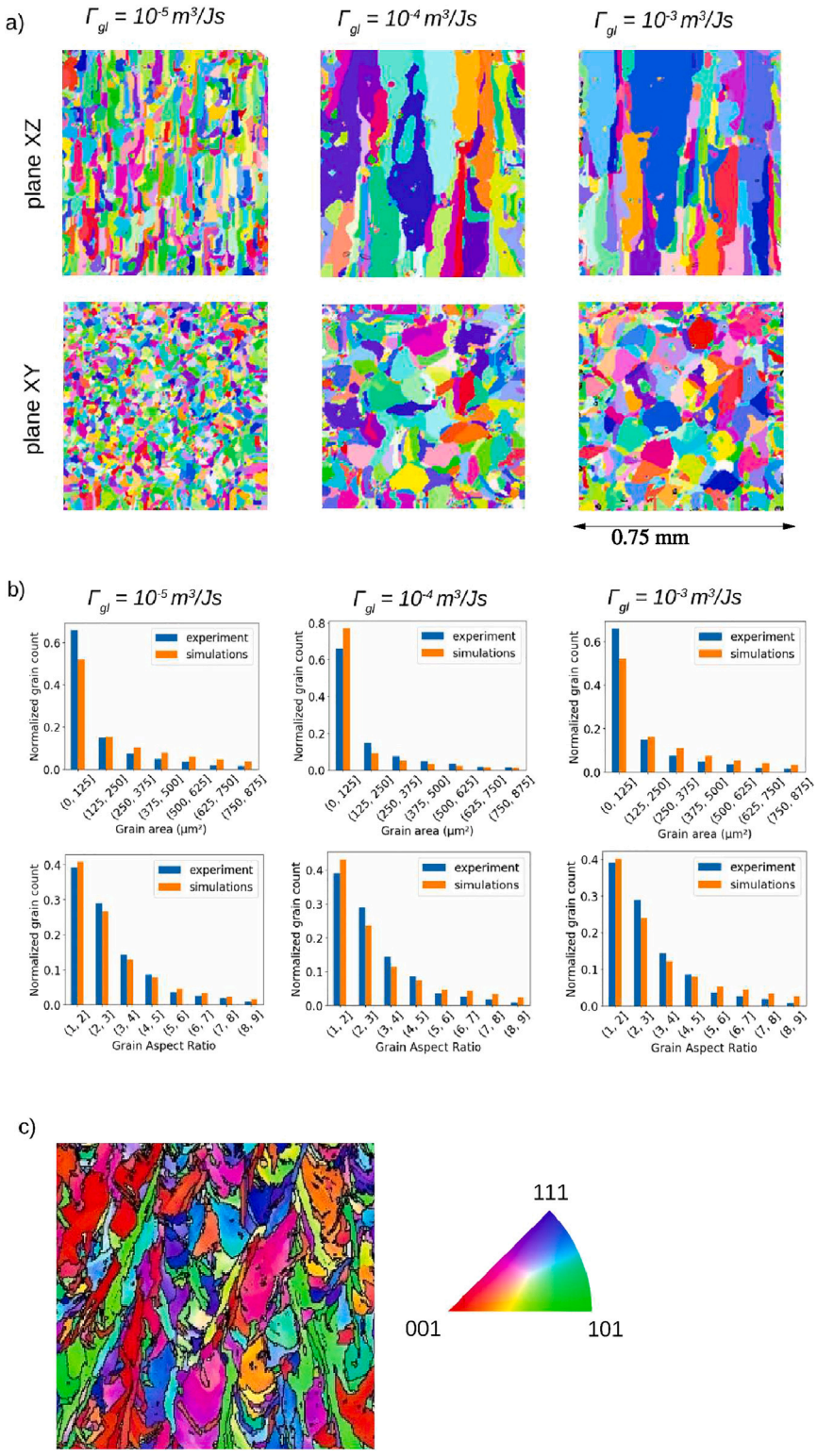

Fig. 4. (a) RVE cross-section after completing full cube deposition (18 layers) using different values of grain–liquid mobility Γ_{gl} and optimal process parameters. Z is the build direction. (b) grain cross-section area and aspect ratio distribution, for experiment (blue) and calculation (orange). The calculations have been performed setting T_b to 600 K. (c) experimental EBSD map. The size of the cross-section in (a) and (c) is the same and equal to 0.75 mm. (For interpretation of the references to color in this figure legend, the reader is referred to the web version of this article.)

the liquid to reach existing solid. Such detrimental effect is further enhanced by the increased hatch spacing, which separates scan tracks away from each other and further limits metallurgical bonding. In this regard, our simulations suggest a distinction between the role of laser power and scan speed on one side, and of hatch spacing on the other side. In fact, while the three terms play the same role in the scalar energy density, comparison of combinations "-++" and "-+-" show a strong variation in porosity when hatch spacing is varied at constant laser power and scan speed. Such effect is larger than, for instance, changing laser power at constant scan speed and hatch spacing, as seen

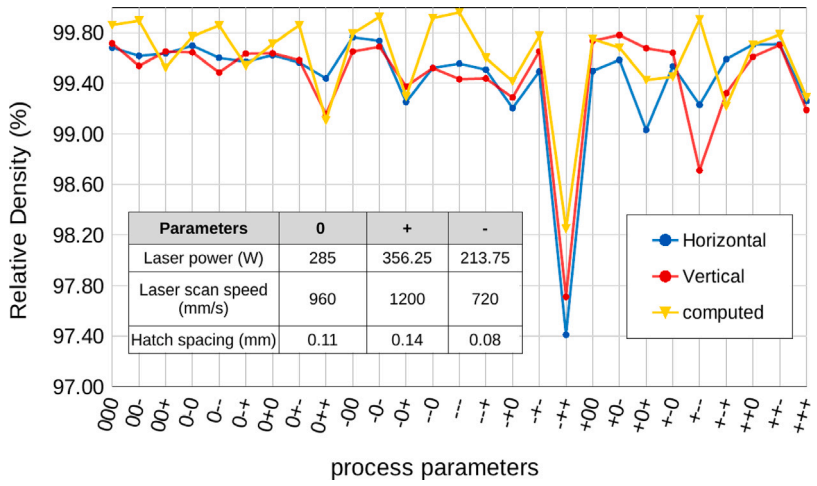

Fig. 5. Comparison of measured and computed relative density for set of process parameters. The process parameters are represented by a sequence of three letters (laser powder, laser speed, hatch spacing), "0" represents printer recommended value, "+" and "-" represented 25% increase and decrease of this value.

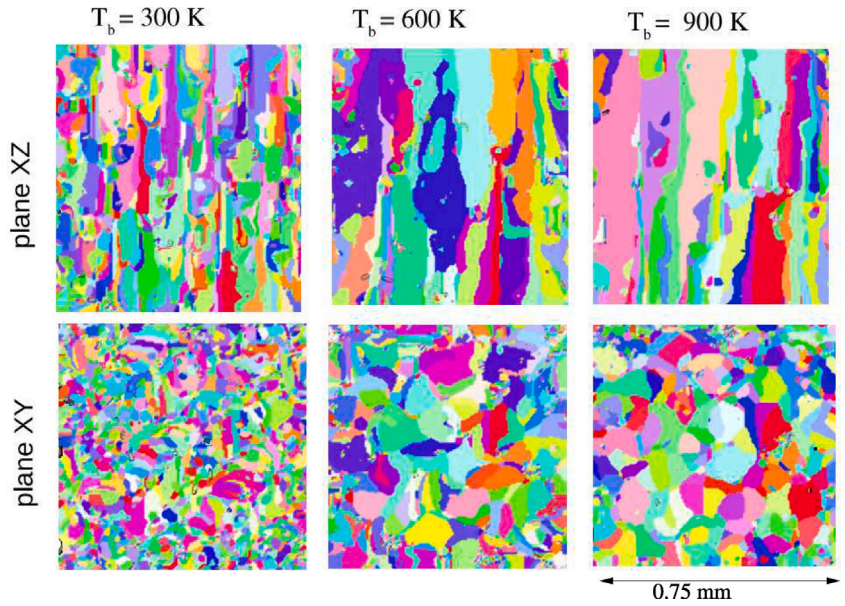

Fig. 6. RVE cross-section after completing full cube deposition (18 layers) for different values of boundary temperature T_b. Z is the build direction.

by comparing "O+-" and "++-" in Fig. 5. Laser power and scan speed seem to affect the size of the melt pool, whereas hatch spacing does not. However it strongly influences the overlap of scan tracks and therefore the ability of the melt pool to reduce porosity by remelting. Therefore, our results highlight remelting as a key factor in controlling porosity.

Next, we explore the effect of the boundary temperature T_b appearing in the heat transfer equation Eq. (25). Such temperature represents the thermal field due to the material surrounding our RVE. The value of T_b is an indication of overall processing temperature during the build. Digital cubes were printed at T_b equal to 300 K, 600 K, 900 K and are presented in Fig. 6. Simulations were run at default process parameters ("OOO"). It is evident that a higher T_b leads to larger and more columnar grains, which can be rationalized considering its influence on the solidification process. In fact, a higher value of T_b reduces liquid undercooling and therefore inhibits nucleation of grains ahead of the solidification front. As a result, epitaxial growth is promoted, resulting in large grains with columnar shape. A similar equiaxed-columnar transition can be triggered by modification of solid–liquid interface mobility, as shown in Fig. 4. Such transition is usually understood in terms of temperature gradient and solid–liquid interface velocity rate [50,51].

Concurrently, larger values of T_b lead to larger melt-pool sizes, which decrease the overall porosity, and conversely a lower value of T_b increases the overall porosity. A good agreement with measured values is seen using T_b equal to 600 K, as shown in Fig. 5. Since the actual value of T_b may depend on the shape and state of the build, our simulations suggest that porosity and grain size and shape may also vary across the build, for complex part geometries.

In order to determine relation between process parameters and microstructure, EBSD characterization was carried out for samples where one parameter was varied while the other two were kept constant. Explicitly, laser power was 213 W and 356 W; scan speed was 1.2 m/s and 0.72 m/s; hatch spacing was 0.14 mm and 0.08 mm at otherwise optimal parameters, resulting in 12 EBSD maps in total. Experiments are compiled in Fig. 7(a–c). In panel (a) of this figure, a low laser power shows smaller grains, with a slightly more equiaxed shape, as compared to the case of high laser power, which presents larger grains with columnar features. Concurrently, porosity is also visible (black spots), confirming lack of fusion porosity at low power and its absence

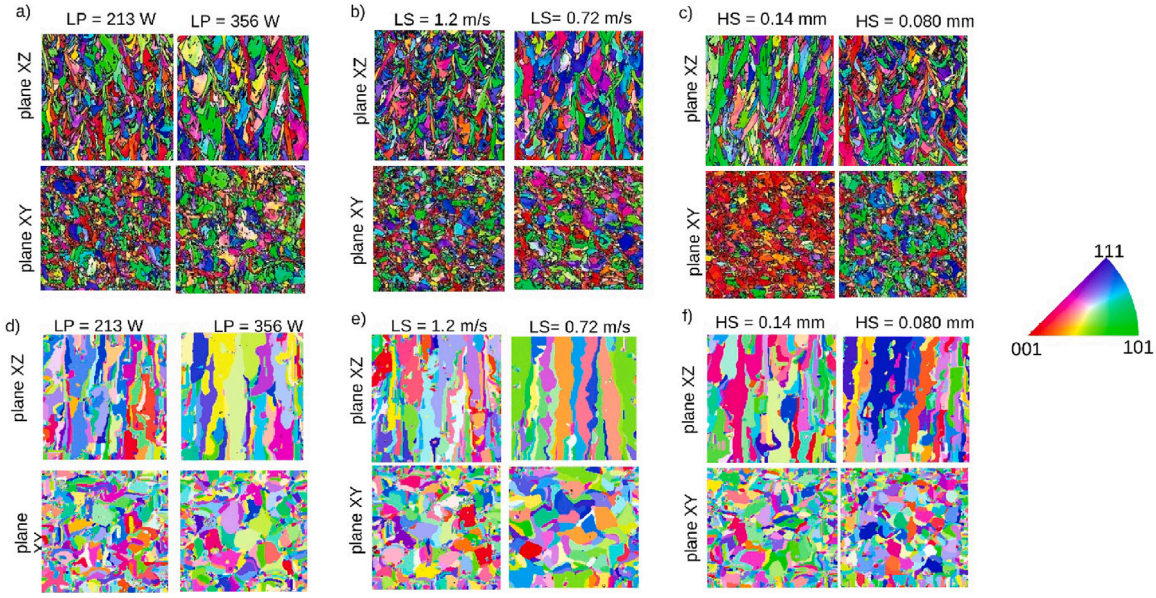

Fig. 7. (a – c) Microstructure characterization of experimental sample built at (a) laser power (LP) 213 W (left) and 356 W (right), (b) laser speed (LS) of 1.2 m/s (left) and 0.72 m/s (right); (c) hatch spacing (HS) of 0.08 mm and 0.14 mm, at otherwise default process parameters; Top: vertical cross-section; Bottom: horizontal cross-section. (d–f) RVE cross-section after completing full cube deposition (18 layers) for (d) laser power of 213 W (left), 356 W (right), (e) scan speed of 1.2 m/s (left) and 0.72 m/s (right), (f) hatch spacing of 0.08 mm and 0.14 mm, at otherwise default process parameters and T_b equal to 600 K.

at high power. In terms of scan speed (Fig. 7(b)), a similar trend is observed whereby high scan speed (low energy density) corresponds to smaller grains with equiaxed microstructure, as compared to the case of low scan speed. Interestingly, variation of hatch spacing does not produce significantly different microstructure (Fig. 7(c)). The experimental maps were assessed by printing digital cubes with the same process parameter combinations, the boundary temperature T_b was set to 600 K. Results are compiled in Fig. 7(d–f) (for a comparison, the microstructure obtained at "optimal" parameters is included in Fig. 6). The digital EBSDs capture the effect of process parameters on microstructure, reproducing trends seen in the experimental EBSD maps. Namely, a variation in laser power and scan speed affects grain size and shape while a variation in hatch spacing has a minor influence on microstructure. However, by directly comparing experimental and computed EBSDs, we see that the latter seems to be more columnar.

The observed enhancement of the columnar features of the grain microstructure with increased absorbed energy density (higher power, lower scan speed) clearly relates to the similar observation discussed in Fig. 6 with respect to the value of boundary temperature T_b. The columnarity of the microstructure is related to the effective temperature around the meltpool, which in fact controls the solidification rate. This temperature affects also the size of the meltpool and its evolution as presented in Fig. 8. Higher power or lower scan speed results in higher average temperature around the melt pool, which is manifested by an increased size and slower decay (after the laser leaves the RVE, "laser OFF" state in Fig. 8), thus promoting epitaxial growth. In other words, our simulations show that, in terms of microstructure control, increasing power input is equivalent to increasing boundary temperature T_b.

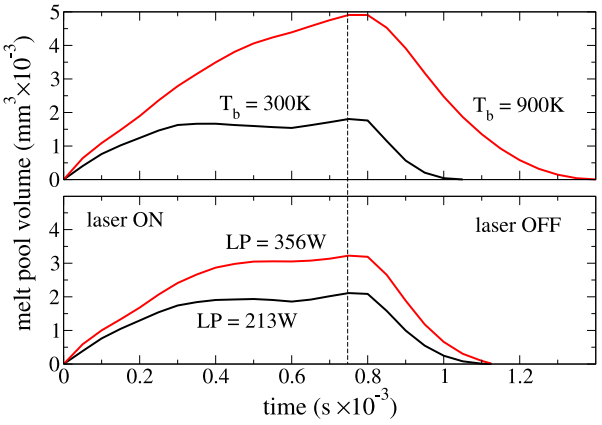

Fig. 8. Melt pool volume evolution for (top) T_b at 300 K and 900 K, and laser power of 286 W; (bottom) laser power of 213 W and 356 W and T_b equal to 600 K. Scan speed was kept at 0.96 m/s. The dashed line separates periods with active and inactive laser heat source.

7. Conclusions

In conclusion, a computational framework was developed by coupling the phase field method with Lattice Boltzmann fluid dynamics solver to model the selective laser melting additive manufacturing process at the scale of the powder in three dimensions, across multiple layers, with the ability to study porosity and microstructure concurrently. The parallel implementation was computationally efficient, requiring moderate computational resources while allowing a cubic computational domain of 0.75 mm^3 to run in about 24 h on 8×24 processors. Model parameters were calibrated at default machine settings, and then the model was used to study the role of process parameters (laser power, scan speed, hatch spacing) on porosity and microstructure across the process window of INCONEL 718. Porosity showed substantial stability across the process window, while the model was able to show good predictions across a wide range of process parameters. At the same time, in terms of microstructure (grain size and shape), the model captured the trend of grain features, including an increase in grain size and aspect ratio with increasing laser power and decreasing scan speed. Interestingly, hatch spacing was found to have a large impact on porosity but a small impact on microstructure, while post processing of the simulation results confirmed this finding. Finally, we would like to point out that concurrent modeling of porosity and microstructure opens interesting avenues to study the influence of process parameters on mechanical properties. In fact, smaller, equiaxed

grains are attractive because of their increased strength (due to Hall–Petch effect) and isotropic properties. However, our result illustrate the inherent coupling between microstructure and porosity, and illustrate that porosity inevitably increases for those desirable microstructures, with an opposite effect on mechanical properties. Such type of investigations strengthen the case for digital modeling as a viable route for digital process assessment and quality control.

CRediT authorship contribution statement

Robert Laskowski: Writing – review & editing, Writing – original draft, Software, Methodology, Investigation, Formal analysis, Data curation, Conceptualization. **Rajeev Ahluwalia:** Writing – review & editing, Methodology. **Gary Teh Wei Hock:** Validation, Data curation. **Choy Sing Ying:** Validation, Data curation. **Chen-Nan Sun:** Validation, Data curation. **Pei Wang:** Validation, Data curation. **Dennis Tan Cheng Cheh:** Validation, Data curation. **Nai Mui Ling Sharon:** Validation, Data curation. **Guglielmo Vastola:** Writing – review & editing, Software, Project administration, Funding acquisition. **Yong-Wei Zhang:** Writing – review & editing, Funding acquisition, Conceptualization.

Declaration of competing interest

The authors declare that they have no known competing financial interests or personal relationships that could have appeared to influence the work reported in this paper.

Data availability

Data will be made available on request.

Acknowledgments

The authors gratefully acknowledge the use of computational resources at the A*STAR Computational Resource Center and the National Supercomputing Center Singapore (NSCC) and the project “Industrial Digital Design and Additive Manufacturing Workflows” (A19E1a0097). Y-WZ acknowledges the support from Singapore A*STAR SERC CRF Award.

References

[1] S. Shah, S. Menon, O.O. Ojo, E. Naghi Ganji, Digitalisation in sustainable manufacturing – a literature review, in: 2020 IEEE International Conference on Technology Management, Operations and Decisions, ICTMOD, 2020, pp. 1–6, http://dx.doi.org/10.1109/ICTMOD49425.2020.9380605.

[2] W. King, A. Anderson, R. Ferencz, N. Hodge, C. Kamath, S. Khairallah, A. Rubenchik, Laser powder bed fusion additive manufacturing of metals; physics, computational, and materials challenges, Appl. Phys. Rev. 2 (2015) 041304.

[3] S. Khairallah, A. Anderson, A. Rubenchik, W. King, Laser powder-bed fusion additive manufacturing: Physics of complex melt flow and formation mechanisms of pores, spatter, and denudation zones, Acta Mater. 108 (2016) 36–45.

[4] S.A. Khairallah, A.A. Martin, J.R.I. Lee, G. Guss, N.P. Calta, J.A. Hammons, M.H. Nielsen, K. Chaput, E. Schwalbach, M.N. Shah, M.G. Chapman, T.M. Willey, A.M. Rubenchik, A.T. Anderson, Y.M. Wang, M.J. Matthews, W.E. King, Controlling interdependent meso-nanosecond dynamics and defect generation in metal 3d printing, Science 368 (6491) (2020) 660–665, http://dx.doi.org/10.1126/science.aay7830, arXiv:https://www.science.org/doi/pdf/10.1126/science.aay7830, URL https://www.science.org/doi/abs/10.1126/science.aay7830.

[5] A. Zakirov, S. Belousov, M. Bogdanova, B. Korneev, A. Stepanov, A. Perepelkina, V. Levchenko, A. Meshkov, B. Potapkin, Predictive modeling of laser and electron beam powder bed fusion additive manufacturing of metals at the mesoscale, Addit. Manuf. 35 (2020) 101236, http://dx.doi.org/10.1016/j.addma.2020.101236, URL https://www.sciencedirect.com/science/article/pii/S2214860420306084.

[6] H. Chen, W. Yan, Spattering and denudation in laser powder bed fusion process: Multiphase flow modelling, Acta Mater. 196 (2020) 154–167, http://dx.doi.org/10.1016/j.actamat.2020.06.033, URL https://www.sciencedirect.com/science/article/pii/S1359645420304687.

[7] R. Ammer, M. Markl, U. Ljungblad, C. Körner, U. Rüde, Simulating fast electron beam melting with a parallel thermal free surface lattice boltzmann method, Comput. Math. Appl. 67 (2) (2014) 318–330, http://dx.doi.org/10.1016/j.camwa.2013.10.001, mesoscopic Methods for Engineering and Science (Proceedings of ICMMES-2012, Taipei, Taiwan, 23–27 2012). URL https://www.sciencedirect.com/science/article/pii/S0898122113005944.

[8] F.-J. Gürtler, M. Karg, K.-H. Leitz, M. Schmidt, Simulation of laser beam melting of steel powders using the three-dimensional volume of fluid method, Physics Procedia 41 (2013) 881–886, http://dx.doi.org/10.1016/j.phpro.2013.03.162, lasers in Manufacturing (LiM 2013). URL https://www.sciencedirect.com/science/article/pii/S1875389213001764.

[9] D. Grange, A. Queva, G. Guillemot, M. Bellet, J.-D. Bartout, C. Colin, Effect of processing parameters during the laser beam melting of inconel 738: Comparison between simulated and experimental melt pool shape, J. Mater Process. Technol. 289 (2021) 116897, http://dx.doi.org/10.1016/j.jmatprotec.2020.116897, URL https://www.sciencedirect.com/science/article/pii/S0924013620303113.

[10] X. Wang, Y. Liu, L. Li, C. Yenusah, Y. Xiao, L. Chen, Multi-scale phase-field modeling of layer-by-layer powder compact densification during solid-state direct metal laser sintering, Mater. Des. 203 (2021) 109615, http://dx.doi.org/10.1016/j.matdes.2021.109615, URL https://www.sciencedirect.com/science/article/pii/S0264127521001684.

[11] C. Körner, M. Markl, J. Koepf, Modeling and simulation of microstructure evolution for additive manufacturing of metals: A critical review, Metall. Mater. Trans. A 51 (2020) 4970–4983, http://dx.doi.org/10.1007/s11661-020-05946-3.

[12] S. Lu, M. Qian, H. Tang, M. Yan, J. Wang, D. StJohn, Massive transformation in ti–6al–4v additively manufactured by selective electron beam melting, Acta Mater. 104 (2016) 303–311.

[13] D. Liu, Y. Wang, Multiphysics simulation of nucleation and grain growth in selective laser melting of alloys, J. Comput. Inf. Sci. Eng. 20 (5) (2020) 051002, http://dx.doi.org/10.1115/1.4046543, arXiv:https://asmedigitalcollection.asme.org/computingengineering/article-pdf/20/5/051002/6647478/jcise_20_5_051002.pdf.

[14] D. Liu, Y. Wang, Mesoscale multi-physics simulation of rapid solidification of ti-6al-4v alloy, Addit. Manuf. 25 (2019) 551–562, http://dx.doi.org/10.1016/j.addma.2018.12.005, URL https://www.sciencedirect.com/science/article/pii/S2214860417306139.

[15] Exaam: Transforming additive manufacturing through exascale simulation, 2021, URL https://www.ornl.gov/project/exaam-transforming-additive-manufacturing-through-exascale-simulation.

[16] J. Koepf, D. Soldner, M. Ramsperger, J. Mergheim, M. Markl, C. Körner, Numerical microstructure prediction by a coupled finite element cellular automaton model for selective electron beam melting, Comput. Mater. Sci. 162 (2019) 148–155, http://dx.doi.org/10.1016/j.commatsci.2019.03.004, URL https://www.sciencedirect.com/science/article/pii/S0927025619301272.

[17] D.-R. Liu, S. Wang, W. Yan, Grain structure evolution in transition-mode melting in direct energy deposition, Mater. Des. 194 (2020) 108919, http://dx.doi.org/10.1016/j.matdes.2020.108919, URL https://www.sciencedirect.com/science/article/pii/S0264127520304536.

[18] R. Shi, S. Khairallah, T. Heo, M. Rolchigo, J. McKeown, M. Matthews, Integrated simulation framework for additively manufactured ti-6al-4v: Melt pool dynamics, microstructure, solid-state phase transformation, and microelastic response, JOM 71 (2019) 3640–3655, http://dx.doi.org/10.1007/s11837-019-03618-1.

[19] M. Yang, L. Wang, W. Yan, Phase-field modeling of grain evolutions in additive manufacturing from nucleation, growth, to coarsening, Npj Comput. Mater. 7 (2021) 56, http://dx.doi.org/10.1038/s41524-021-00524-6.

[20] N. Moelans, B. Blanpain, P. Wollants, Quantitative analysis of grain boundary properties in a generalized phase field model for grain growth in anisotropic systems, Phys. Rev. B 78 (2008) 024113, http://dx.doi.org/10.1103/PhysRevB.78.024113, URL https://link.aps.org/doi/10.1103/PhysRevB.78.024113.

[21] J. Heulens, B. Blanpain, N. Moelans, A phase field model for isothermal crystallization of oxide melts, Acta Mater. 59 (5) (2011) 2156–2165, http://dx.doi.org/10.1016/j.actamat.2010.12.016, URL https://www.sciencedirect.com/science/article/pii/S1359645410008372.

[22] S. Chatterjee, N. Moelans, A grand-potential based phase-field approach for simulating growth of intermetallic phases in multicomponent alloy systems, Acta Mater. 206 (2021) 116630, http://dx.doi.org/10.1016/j.actamat.2021.116630, URL https://www.sciencedirect.com/science/article/pii/S1359645421000100.

[23] I. Steinbach, Phase-field models in materials science, Modelling Simulation Mater. Sci. Eng. 17 (7) (2009) 073001, http://dx.doi.org/10.1088/0965-0393/17/7/073001.

[24] B. Radhakrishnan, S.B. Gorti, J.A. Turner, R. Acharya, J.A. Sharon, A. Staroselsky, T. El-Wardany, Phase field simulations of microstructure evolution in in718 using a surrogate ni–fe–nb alloy during laser powder bed fusion, Metals 9 (1) (2019) http://dx.doi.org/10.3390/met9010014, URL https://www.mdpi.com/2075-4701/9/1/14.

[25] C.A. Gandin, M. Rappaz, R. Tintillier, 3-dimensional simulation of the grain formation in investment castings, Metall. Mater. Trans. A 25 (3) (1994) 629–635, http://dx.doi.org/10.1007/BF02651604.

[26] H. Dong, P. Lee, Simulation of the columnar-to-equiaxed transition in directionally solidified al–cu alloys, Acta Mater. 53 (3) (2005) 659–668, http://dx.doi.org/10.1016/j.actamat.2004.10.019, URL https://www.sciencedirect.com/science/article/pii/S1359645404006287.

[27] J.-H. Cho, S.-J. Na, Implementation of real-time multiple reflection and fresnel absorption of laser beam in keyhole, J. Phys. D: Appl. Phys. 39 (24) (2006) 5372–5378, http://dx.doi.org/10.1088/0022-3727/39/24/039.

[28] W. Tan, N.S. Bailey, Y.C. Shin, Investigation of keyhole plume and molten pool based on a three-dimensional dynamic model with sharp interface formulation, J. Phys. D: Appl. Phys. 46 (5) (2013) 055501, http://dx.doi.org/10.1088/0022-3727/46/5/055501.

[29] D. Grange, A. Queva, G. Guillemot, M. Bellet, J.-D. Bartout, C. Colin, Effect of processing parameters during the laser beam melting of inconel 738: Comparison between simulated and experimental melt pool shape, J. Mater Process. Technol. 289 (2021) 116897, http://dx.doi.org/10.1016/j.jmatprotec.2020.116897, URL https://www.sciencedirect.com/science/article/pii/S0924013620303113.

[30] T. Krüger, H. Kusumaatmaja, A. Kuzmin, O. Shardt, G. Silva, E. Magnus Viggen, The Lattice Boltzmann Method Principles and Practice, Springer International Publishing Switzerland, 2017.

[31] Z. Guo, B. Shi, N. Wang, Lattice bgk model for incompressible navier-stokes equation, J. Comput. Phys. 165 (1) (2000) 288–306, http://dx.doi.org/10.1006/jcph.2000.6616, URL https://www.sciencedirect.com/science/article/pii/S0021999100966166.

[32] A. Fakhari, T. Mitchell, C. Leonardi, D. Bolster, Improved locality of the phase-field lattice-boltzmann model for immiscible fluids at high density ratios, Phys. Rev. E 96 (2017) 053301, http://dx.doi.org/10.1103/PhysRevE.96.053301, URL https://link.aps.org/doi/10.1103/PhysRevE.96.053301.

[33] Y.Q. Zu, S. He, Phase-field-based lattice boltzmann model for incompressible binary fluid systems with density and viscosity contrasts, Phys. Rev. E 87 (2013) 043301, http://dx.doi.org/10.1103/PhysRevE.87.043301, URL https://link.aps.org/doi/10.1103/PhysRevE.87.043301.

[34] D. Jacqmin, Calculation of two-phase navier–stokes flows using phase-field modeling, J. Comput. Phys. 155 (1) (1999) 96–127, http://dx.doi.org/10.1006/jcph.1999.6332, URL https://www.sciencedirect.com/science/article/pii/S0021999199963325.

[35] Q. Li, K.H. Luo, Y.J. Gao, Y.L. He, Additional interfacial force in lattice boltzmann models for incompressible multiphase flows, Phys. Rev. E 85 (2012) 026704, http://dx.doi.org/10.1103/PhysRevE.85.026704, URL https://link.aps.org/doi/10.1103/PhysRevE.85.026704.

[36] C. Körner, M. Thies, T. Hofmann, N. Thürey, U. Rüde, Lattice boltzmann model for free surface flow for modeling foaming, J. Stat. Phys. 121 (2005) 179–196, http://dx.doi.org/10.1007/s10955-005-8879-8.

[37] H. Chen, C. Teixeira, K. Molvig, Realization of fluid boundary conditions via discrete boltzmann dynamics, Internat. J. Modern Phys. C 09 (08) (1998) 1281–1292, http://dx.doi.org/10.1142/S0129183198001151.

[38] A.J.C. Ladd, Numerical simulations of particulate suspensions via a discretized boltzmann equation, part 1. theoretical foundation, J. Fluid Mech. 271 (1994) 285–309, http://dx.doi.org/10.1017/S0022112094001771.

[39] X. He, Q. Zou, L.-S. Luo, M. Dembo, Analytic solutions of simple flows and analysis of nonslip boundary conditions for the lattice boltzmann bgk model, J. Stat. Phys. 87 (1997) 115–136, http://dx.doi.org/10.1007/BF02181482.

[40] D.R. Noble, J.R. Torczynski, A lattice-boltzmann method for partially saturated computational cells, Internat. J. Modern Phys. C 09 (08) (1998) 1189–1201, http://dx.doi.org/10.1142/S0129183198001084.

[41] O.E. Strack, B.K. Cook, Three-dimensional immersed boundary conditions for moving solids in the lattice-boltzmann method, Internat. J. Numer. Methods Fluids 55 (2) (2007) 103–125, http://dx.doi.org/10.1002/fld.1437, arXiv:https://onlinelibrary.wiley.com/doi/pdf/10.1002/fld.1437 URL https://onlinelibrary.wiley.com/doi/abs/10.1002/fld.1437.

[42] I. Ginzburg, F. Verhaeghe, D. d'Humiéres, Two-relaxation-time lattice boltzmann scheme: About parametrization, velocity, pressure and mixed boundary conditions, Commun. Comput. Phys. 3 (2) (2008) 427–478.

[43] D. d'Humières, I. Ginzburg, Viscosity independent numerical errors for lattice boltzmann models: From recurrence equations to magic collision numbers, Comput. Math. Appl. 58 (5) (2009) 823–840, mesoscopic Methods in Engineering and Science.

[44] I. Ginzburg, F. Verhaeghe, D. d'Humiéres, Study of simple hydrodynamic solutions with the two-relaxation-times lattice boltzmann scheme, Commun. Comput. Phys. 3 (3) (2008) 519–581.

[45] Q.B. Nguyen, M.L.S. Nai, Z. Zhu, C.-N. Sun, J. Wei, W. Zhou, Characteristics of inconel powders for powder-bed additive manufacturing, Engineering 3 (5) (2017) 695–700, http://dx.doi.org/10.1016/J.ENG.2017.05.012, URL https://www.sciencedirect.com/science/article/pii/S209580991730721X.

[46] [link]. URL https://www.azom.com/.

[47] A. Agazhanov, D. Samoshkin, Y. Kozlovskii, Thermophysical properties of inconel 718 alloy, J. Phys. Conf. Ser. 1382 (2019) 012175, http://dx.doi.org/10.1088/1742-6596/1382/1/012175.

[48] [link]. URL https://www.nuclear-power.net/nickel-specific-heat-latent-heat-vaporization-fusion/.

[49] R.F. Brooks, A.P. Day, R.J.L. Andon, L.A. Chapman, K.C. Mills, P.N. Quested, Measurement of viscosities of metals and alloys with an oscillating viscometer, 15 ECTP Proceed. 33 (2001) 73.

[50] S.A. Nabavizadeh, M. Eshraghi, S.D. Felicelli, Three-dimensional phase field modeling of columnar to equiaxed transition in directional solidification of inconel 718 alloy, J. Cryst. Growth 549 (2020) 125879, http://dx.doi.org/10.1016/j.jcrysgro.2020.125879, URL https://www.sciencedirect.com/science/article/pii/S0022024820304024.

[51] G. Knapp, N. Raghavan, A. Plotkowski, T. DebRoy, Experiments and simulations on solidification microstructure for inconel 718 in powder bed fusion electron beam additive manufacturing, Addit. Manuf. 25 (2019) 511–521, http://dx.doi.org/10.1016/j.addma.2018.12.001, URL https://www.sciencedirect.com/science/article/pii/S2214860418306973.